Available online at www.sciencedirect.com
ScienceDirect
International Journal of Thermal Sciences 48 (2009) 461–474
International Journal of Thermal Sciences
www.elsevier.com/locate/ijts

Mixed convection flow past a vertical plate: Stability analysis and its direct simulation

K. Venkatasubbaiah [a], T.K. Sengupta [b,*]

[a] *Department of Aerospace Engineering, IIT Kanpur, Currently at Amrita School of Engineering, Coimbatore, India*
[b] *Department of Aerospace Engineering, Indian Institute of Technology Kanpur, Kanpur 208016, India*

Received 18 March 2008; accepted 18 March 2008

Available online 25 April 2008

Abstract

Stability of mixed convection flow past vertical flat plate have been investigated here using compound matrix method (CMM) to solve linearized equations arising out of a spatial analysis and by direct numerical simulation (DNS) using a Boussinesq approximation. CMM is applied to study spatial stability of mixed convection flow past a vertical plate. A double loop in the neutral curve is shown in the forced convection limit of opposing flows for the first time. To check this and other observations of the linear analysis, two-dimensional Navier–Stokes equations are also solved here with the buoyancy term represented by the Boussinesq approximation. This type of receptivity study, by direct simulation have been extended here for mixed convection flows. Also, we establish the presence of a spatio-temporally growing wave-front for this flow—that was shown to exist in Sengupta et al. [T.K. Sengupta, A.K. Rao, K. Venkatasubbaiah, Spatio-temporal growing wave-fronts in spatially stable boundary layers, Phys. Rev. Lett. 96 (224504) (2006) 1–4; T.K. Sengupta, A.K.Rao, K. Venkatasubbaiah, Spatio-temporal growth of disturbances in a boundary layer and energy based receptivity analysis, Phys. of Fluids 18 (094101) (2006) 1–9] for boundary layer developing over a horizontal flat plate in the absence of heat transfer.

Keywords: Mixed convection flow; Linear and nonlinear stability; Nonlinear receptivity; Direct numerical simulation; Compound matrix method

1. Introduction

Despite significant advances made in hydrodynamic stability theory, there are many issues of flow transition (those affected by more than one physical mechanisms or due to the presence of simultaneous multiple unstable modes), remain incompletely understood. Mixed convection flow is a typical example, seen in many engineering devices. In pure hydrodynamic scenario, flow instabilities are caused due to complex interactions between inertial and viscous mechanisms of exchanging momentum-detailed description of the same are given in Drazin and Reid [3]. When heat transfer effects are included, ensuing instability requires taking into consideration of energy transfer, along with the added buoyancy-induced effects in momentum conservation equation. These added effects make the corresponding flow instability studies further complicated. A comprehensive review of heat transfer aspect of mixed convection are given in Gebhart et al. [4]. It has been noted by Brewster and Gebhart [5] that in the mixed convection regime, instability is due to growth of small disturbances that can be studied by linearized governing equation. Such an approach for instability of flows over a horizontal plate with heat transfer have been studied in Wu and Cheng [6], Chen and Mucoglu [7], Sengupta and Venkatasubbaiah [8] and other references contained therein. In Sengupta and Venkatasubbaiah [8], it has been shown that there exist a critical buoyancy parameter, above which a very unstable higher frequency variation ensues, in addition to the pure hydrodynamic mode characterized by lower frequency disturbances. Both of these modes for the flow past heated horizontal plates were obtained by the linearized spatial stability analysis performed using CMM. For the first time, existence of critical buoyancy parameter was shown theoretically that has been detected in the experiments by Wang [9] earlier.

* Corresponding author.
E-mail addresses: k_vnekatasubbaiah@ettimadai.amrita.edu (K. Venkatasubbaiah), tksen@iitk.ac.in (T.K. Sengupta).

1290-0729/$ – see front matter
doi:10.1016/j.ijthermalsci.2008.03.019

Nomenclature

Re	Reynolds number	k	non-dimensional wave number
Gr	Grashof number	β_0	non-dimensional circular frequency
Pr	Prandtl number	ψ	stream function
Ri_x	Buoyancy parameter	ω	vorticity
δ^*	displacement thickness	F_f	non-dimensional frequency parameter

For flow past vertical plates, induced body force due to heat transfer is either parallel or anti-parallel to the mean convection direction—as shown schematically in Fig. 1. These are commonly referred to as assisting and opposing flows. Like other convection dominated unseparated flows, instability of mixed convection flow past vertical plates also occur via growth of small disturbances. Thus, this has been studied by linear analysis in Mucoglu and Chen [10], Brewstar and Gebhart [5] and Moresco and Healey [11]. These analyses have been traditionally performed using temporal theory (see, e.g., Mucoglu and Chen [10]). The equilibrium assisting flow was obtained by local non-similarity method and it was noted that the buoyancy force stabilizes the flow. However, experimental studies show the instability to be related to spatial growth of disturbances when the flow is excited by fixed frequency sources. Hence a spatial theory is preferred to study the stability of mixed convection flows, as in Lee et al. [12]. They reported results for the buoyancy parameter $Ri_x = Gr_x/Re_x^2$ in the range between zero and infinity, where Gr_x and Re_x are the Grashof and Reynolds numbers based on current length. Lee et al. [12] and Moresco and Healey [11] have studied mixed convection flow over the entire range of Ri_x, but reported two unstable modes of disturbance for natural convection dominated flows only. In the present work, existence of two unstable modes and therefore two loops of neutral curve is established in the forced convection regime.

Additionally, in the present study we focus upon both the linear and nonlinear route of instability to fixed frequency wall excitations. First, the linear spatial stability results for mixed convection flow past vertical plate are reported using CMM to solve the stability equations. CMM allows circumventing the *stiffness* that is inherent with viscous instability problems. Detailed description of CMM is to be found in Drazin and Reid [3], Allen and Bridges [13,14] and Sengupta and Venkatasubbaiah [8] and its use for mixed convection flow past vertical plate is reported here for the first time. All these stability analyses suffer from the restriction of either nonlinearity or nonparallelism of the mean flow or due to both.

Qualitative and quantitative differences exist between the linear spatial theory and experimental results for flows with and without heat transfer. For flows without heat transfer, Fasel and Konzelmann [15] have studied effects based on solution of complete Navier–Stokes equation to include all possible nonparallel and nonlinear effects. This represents direct numerical simulation (DNS) of the laboratory experiments of Schubauer and Skramstad [16], where the response of the boundary layer to a vibrating ribbon at different frequencies were investigated.

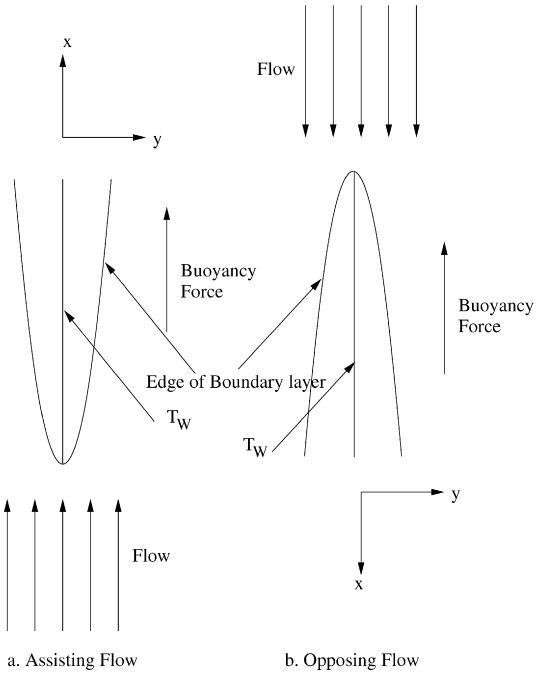

Fig. 1. Mixed convection flow over a vertical flat plate.

So far, no such studies have been undertaken for mixed convection flows. In the present exercise we also report the complete nonlinear, nonparallel analysis of mixed convection flow past vertical plates by solving the time-dependent Navier–Stokes equation. In flows with heat transfer, Lee et al. [17] have reported nonparallel instability studies for flow over inclined heated platefrom vertical to horizontal position. They used a nonparallel formulation based on an order-of-magnitude analysis. However, it is necessary to evaluate the results of the paper closely. For example, the critical Reynolds number (Re_{cr}) value attributed to experimental results in Schubauer and Skramstad [16] is erroneously given as $Re_{cr} = 378$, whereas, Fig. 11 of Schubauer and Skramstad [16] clearly shows this to be in excess of 400. Lee et al. [17] have calculated this as $Re_{cr} = 374$ and claimed excellent agreement with experiment. They also obtained this Re_{cr} for $F_f = \beta_0 \nu / U_\infty^2 = 63.61 \times 10^{-6}$, that is more than six times lower than the actual value given in Schubauer and Skramstad [16]. Here, β_o is the circular frequency of wall-excitation; ν is the kinematic viscosity and U_∞ is the boundary layer edge velocity. In a critique of early nonparallel methods, Tumin [18] cites neglecting the dependence of eigen functions on streamwise coordinate as responsible for the discrepancy. He used the theory of multiple scales to incor-

porate nonparallel effects for both traveling wave and stationary longitudinal-vortices mode solutions. Stabilizing effects due to nonparallelism of the mean flow was reported by Tumin [18]. Thus, the past studies have not been able to provide correct Re_{cr} at the correct F_f, based on linearized quasi-parallel and weakly nonparallel models for the stability properties of mixed convection flows.

Present study attempts to investigate the linearized parallel spatial stability of the mixed convection assisting and opposing flows in the forced convection limit by using CMM and to study nonparallel, nonlinear stability of the same based on the solution of complete Navier–Stokes and energy equations to include all possible effects for two-dimensional flows. We have used the wall excitation model of Fasel and Konzelmann [15] for the DNS of mixed convection flow over the vertical plate.

The paper is structured in the following manner. Governing equations are given in the next section. Linear stability analysis is discussed in Section 3. Direct numerical simulation of the flow is reported in Section 4. The paper closes with a summary and some comments in Section 5.

2. The governing equations

We consider the laminar two-dimensional motion of fluid past a semi-infinite vertical plate, with the free stream velocity and temperature denoted by, U_∞ and T_∞. The flow configurations for assisting and opposing flows are shown in Fig. 1. We consider the flow over isothermal vertical plate, for which the surface temperature (T_w) is greater than the free stream temperature (T_∞). Governing equations are presented in non-dimensional form with the buoyancy term modeled by the Boussinesq approximation. Non-dimensionalization of equations are performed by introducing an appropriate length (L), velocity (U_∞), temperature ($\Delta T = T_w - T_\infty$) and pressure scales ($\rho U_\infty^2$). These equations for the velocity and temperature fields are as given in Gebhart et al. [4],

$$\nabla \cdot \vec{V} = 0 \tag{1}$$

$$\frac{D\vec{V}}{Dt} = \pm\frac{Gr}{Re^2}T - \nabla p + \frac{1}{Re}\nabla^2\vec{V} \tag{2}$$

$$\frac{DT}{Dt} = \frac{1}{Re\,Pr}\nabla^2 T \tag{3}$$

where $T = (T^* - T_\infty)/\Delta T$ and $Gr = g\beta_t \Delta T L^3/\nu^2$; $Re = U_\infty L/\nu$ and $Pr = \nu/\alpha$ where α is the thermal diffusivity of the fluid; T^* is the dimensional temperature in the field. In the momentum conservation equation, the quantity Gr/Re^2, is also known as the Richardson number (Ri). Positive and negative signs of Ri refer to assisting and opposing flows, respectively. The Grashof number weighs the relative importance of buoyancy and viscous diffusion terms and in the mixed convection regime, Ri is of order one.

3. Linear stability analysis

For studying linear instability of mixed convection flow over a vertical flat plate, equilibrium and disturbance fields are separated and their equations are similar to that obtained in Sengupta and Venkatasubbaiah [8] and only essential details are given below.

3.1. Equilibrium or mean flow equations

The mean flow equations are obtained by invoking boundary layer approximation for two-dimensional steady incompressible flow with constant properties and Boussinesq approximation. The mean flow equations are obtained using the following variables: $\eta_s = y\sqrt{U_\infty/\nu x}$ for the independent variable; $u/U_\infty = F'$ and $(T^* - T_\infty)/(T_w - T_\infty) = T$ for the dependent variables and are obtained from the solution of (Oosthuizen and Naylor [19]),

$$F''' + \frac{FF''}{2} \pm Ri_x T = 0 \tag{4}$$

$$T'' + \frac{Pr}{2}FT' = 0 \tag{5}$$

where $Ri_x = Gr_x/Re_x^2$ is the buoyancy parameter and $\pm$ signs are for the buoyancy term for assisting and opposing flows, respectively. In these equations, primes indicate derivatives with respect to η_s. As Ri_x is a function of x, similarity solution does not exist. However, if Ri_x is small, then one can obtain the perturbation solution by representing the dependent variables by,

$$F = F_0 + Ri_x F_1 + (Ri_x)^2 F_2 + \cdots$$
$$T = \theta_0 + Ri_x\theta_1 + (Ri_x)^2\theta_2 + \cdots$$

where F_0 and θ_0 are the solution for pure forced convection cases for $Ri_x = 0$. Thus, a formal perturbation series analysis provides the governing equations for the mean flow as given by the following sets of equations—expressed for up to second order only,

$$F_0''' + \frac{F_0F_0''}{2} = 0 \tag{6}$$

$$F_1''' + \frac{F_0F_1''}{2} + \frac{F_1F_0''}{2} \pm \theta_0 = 0 \tag{7}$$

$$F_2''' + \frac{F_0F_2''}{2} + \frac{F_1F_1''}{2} + \frac{F_2F_0''}{2} \pm \theta_1 = 0 \tag{8}$$

$$\theta_0'' + \frac{Pr}{2}F_0\theta_0' = 0 \tag{9}$$

$$\theta_1'' + \frac{Pr}{2}F_0\theta_1' + \frac{Pr}{2}F_1\theta_0' = 0 \tag{10}$$

$$\theta_2'' + \frac{Pr}{2}F_0\theta_2' + \frac{Pr}{2}F_1\theta_1' + \frac{Pr}{2}F_2\theta_0' = 0 \tag{11}$$

These equations are solved subject to the boundary conditions at $\eta_s = 0$: $F_0 = F_0' = F_1 = F_1' = F_2 = F_2' = 0$ and $\theta_0 = 1$, $\theta_1 = \theta_2 = 0$ and as $\eta_s \to \infty$: $F_0' = 1$, $F_1' = F_2' = 0$ and $\theta_0 = \theta_1 = \theta_2 = 0$.

The mean flow in air is obtained by solving Eqs. (6) to (11) by the four-stage Runge–Kutta method using shooting technique with $Pr = 0.7$, and by taking maximum co-ordinate, $(\eta_s)_{\max} = 12$ divided into 4000 equal sub-intervals. For different Re and Ri_x, mean flow solutions are obtained for assisting and opposing flows. Non-dimensional velocity and temperature

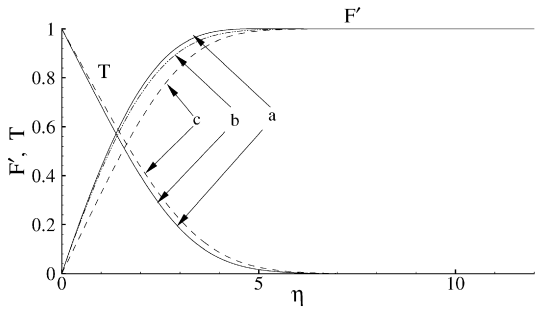

Fig. 2. Mean flow profiles for assisting (with $Ri_x = 0.1$) and opposing (with $Ri_x = 0.001$) flows given by (a) first order perturbation solution for assisting flow; (b) second order perturbation solution for assisting flow and (c) first order perturbation solution for opposing flow.

profiles are as shown in Fig. 2, obtained up to second order accuracy, for the assisting (with $Ri_x = 0.1$) and opposing flows (with $Ri_x = 0.001$). There is only a small deviation between the first and second order quantities for the velocity field for the assisting flow at the high value of $Ri_x = 0.1$. Stability studies conducted here are for lower Ri_x values, for which higher order effects will be further negligible. We will also show that the stability of the two mean flows of a and b in Fig. 2, have negligible difference for the eigenvalues and the eigen-spectrum. Here, we do not see any difference in the temperature distribution inside the boundary layer, when the second order terms are added.

3.2. Stability equations

Here, linear stability equations for two-dimensional mixed convection flow over a vertical plate have been derived by starting from the non-dimensional equations (1) to (3). All physical variables are split into the mean (given by Eqs. (6) to (11)) and the disturbance components in the following,

$$u(x,y,t) = \bar{U}(x,y) + \epsilon u_d(x,y,t)$$
$$v(x,y,t) = \bar{V}(x,y) + \epsilon v_d(x,y,t)$$
$$p(x,y,t) = \bar{P}(x,y) + \epsilon p_d(x,y,t)$$
$$T(x,y,t) = \bar{T}(x,y) + \epsilon T_d(x,y,t)$$

with ϵ as the non-dimensionalizing small parameter of the problem. Stability equations are obtained by making additional parallel flow assumption ($\bar{U} = \bar{U}(y)$, $\bar{V} = 0$ and $\bar{T} = \bar{T}(y)$), so that a normal mode spatial instability analysis is possible by looking for a solution of the linearized equations of the following form:

$$[u_d, v_d, p_d, T_d] = \big[f(y), \phi(y), \pi(y), h(y)\big] e^{i(kx - \beta_0 t)} \tag{12}$$

For the spatial analysis, one fixes a real frequency that is indicated here by β_0. After substituting Eq. (12) into Eqs. (1) to (3) and simplifying, one obtains the following system of equations for disturbance quantities,

$$i(k\bar{U} - \beta_0)(k^2\phi - \phi'') + ik\bar{U}''\phi = \pm\frac{Gr}{Re^2} ikh' - \frac{1}{Re}(\phi^{iv} - 2k^2\phi'' + k^4\phi) \tag{13}$$

$$i(k\bar{U} - \beta_0)h + \bar{T}'\phi = \frac{1}{Re\,Pr}(h'' - k^2 h) \tag{14}$$

In deriving these equations, length scale (L) is chosen as the displacement thickness (δ^*) of the boundary layer. These are the well-known Orr–Sommerfeld equations for mixed convection flows, governing the amplitudes of disturbance normal velocity and temperature field. Here, primes denote differentiation with respect to y. Eqs. (13) and (14) are to be solved subject to the six boundary conditions:

$$\text{at } y = 0: \quad \phi, \phi' = 0 \quad \text{and} \quad h = 0 \tag{15}$$

$$\text{as } y \to \infty: \quad \phi, \phi', h \to 0 \tag{16}$$

Homogeneous boundary condition for h at the wall corresponds to eigenvalue analysis. In contrast, for receptivity analyses, $h = h(y = 0, t)$ is prescribed at the wall, representing a specific thermal input. As shown earlier in Sengupta et al. [20], these two analyses are related through the disturbance amplitude expression for linear systems. Eqs. (13) and (14), together with the boundary conditions (15) and (16), reveal that the temperature field, as given by Eq. (14), decouples from the velocity field in the free stream ($y \to \infty$), as $\bar{T}' \approx 0$ there. Thus, the characteristic modes at free stream are given by: $\lambda_{5,6} = \mp S$, where $S = [k^2 + iRe\,Pr(k - \beta_0)]^{1/2}$. However, the disturbance momentum equation is not decoupled, as Eq. (13) at the free stream simplifies (with $\bar{U} = 1$ and mean flow derivatives as zero) to,

$$i(k - \beta_0)(k^2\phi - \phi'') = \pm\frac{Gr}{Re^2} ikh' - \frac{1}{Re}(\phi^{iv} - 2k^2\phi'' + k^4\phi) \tag{17}$$

This equation for the disturbance amplitude of normal component of velocity represents a forced dynamics, with the thermal field providing the forcing. The homogeneous part of the solution is governed by the following characteristic exponents, $\lambda_{1,2} = \mp k$ and $\lambda_{3,4} = \mp Q$, where $Q^2 = k^2 + iRe(k - \beta_0)$. Out of these six characteristic values, we discard those modes that grow with y in CMM. Thus, the admissible fundamental solution components are given by,

$$\phi_1 = e^{-ky}; \qquad \phi_3 = e^{-Qy} \quad \text{and} \quad \phi_5 = e^{-Sy} \tag{18}$$

when the real part of k, Q and S are all positive. We represent the governing stability equations as a set of six first order ordinary differential equations by introducing the vector: $\mathbf{u}(y,.) = [u_1(y,.), u_2(y,.), u_3(y,.), u_4(y,.), u_5(y,.), u_6(y,.)]^T$. Where, $u_1 = \phi$, $u_2 = \phi'$, $u_3 = \phi''$, $u_4 = \phi'''$, $u_5 = h$ and $u_6 = h'$. The governing system of equations given by Eqs. (13) and (14) can be written as,

$$\{u_j'\} = [A]\{u_j\} \tag{19}$$

where the non-zero elements of the matrix A are given by, $a_{12} = 1$, $a_{23} = 1$, $a_{34} = 1$, $a_{41} = -a$, $a_{43} = b$, $a_{46} = c$, $a_{56} = 1$, $a_{61} = e$, $a_{65} = d$; with $a = k^4 + iRek\bar{U}'' + iRek^2(k\bar{U} - \beta_0)$; $b = 2k^2 + iRe(k\bar{U} - \beta_0)$; $c = \pm ikGr/Re$; $d = k^2 + iRe\,Pr(k\bar{U} - \beta_0)$ and $e = Re\,Pr\bar{T}'$.

These equations are further modified for CMM, details of which can be obtained in Sengupta and Venkatasubbaiah [8]. One obtains the induced system equations for the present problem as,

$$y_1' = y_2 \tag{20}$$
$$y_2' = by_1 + cy_4 + y_5 \tag{21}$$
$$y_3' = y_4 + y_6 \tag{22}$$
$$y_4' = dy_3 + y_7 \tag{23}$$
$$y_5' = cy_7 + y_{11} \tag{24}$$
$$y_6' = y_7 + y_8 + y_{12} \tag{25}$$
$$y_7' = dy_6 + y_9 + y_{13} \tag{26}$$
$$y_8' = by_6 + y_9 - cy_{10} + y_{14} \tag{27}$$
$$y_9' = by_7 + dy_8 + y_{15} \tag{28}$$
$$y_{10}' = y_{16} \tag{29}$$
$$y_{11}' = -ay_1 + cy_{13} \tag{30}$$
$$y_{12}' = y_{13} + y_{14} \tag{31}$$
$$y_{13}' = ey_1 + dy_{12} + y_{15} \tag{32}$$
$$y_{14}' = ay_3 + by_{12} + y_{15} - cy_{16} + y_{17} \tag{33}$$
$$y_{15}' = ey_2 + ay_4 + by_{13} + dy_{14} + y_{18} \tag{34}$$
$$y_{16}' = ey_3 + y_{19} \tag{35}$$
$$y_{17}' = ay_6 + y_{18} - cy_{19} \tag{36}$$
$$y_{18}' = ey_5 + ay_7 + dy_{17} \tag{37}$$
$$y_{19}' = ey_6 + y_{20} \tag{38}$$
$$y_{20}' = ey_8 - ay_{10} + by_{19} \tag{39}$$

where the primes indicate differentiation with respect to y, the wall-normal coordinate. We note that the usage of asymptotic boundary conditions at $y = Y_\infty$ allows us to convert the original boundary value problem to an initial value problem, with the initial conditions as given in Sengupta and Venkatasubbaiah [8].

Main aim of the instability study is to identify critical parameters that mark the onset of instability, i.e. to obtain Re_{cr} and the corresponding circular frequency, β_{cr}. Here we present results for some representative cases that will be used to compare with DNS results. Neutral curves for assisting and opposing flows are shown in Figs. 3 and 4, respectively. Critical parameters for assisting and opposing flows are tabulated and shown in Tables 1 and 2.

In Fig. 3(a), the neutral curve for the case of $Ri_x = 0.0$, i.e. for the Blasius profile is shown—that is computed here to validate the present formulation and method with the results reported earlier in Sengupta et al. [20]. The essential difference between the two methods lies in the fact that we solve the complete set of disturbance equation here (both Eqs. (13) and (14)), as compared to that in Sengupta et al. [20], where only Eq. (13) was solved by CMM. The calculated eigenvalues (as shown in tabulated form in Sengupta and Venkatasubbaiah [8]) match exactly with that in Sengupta et al. [20]. Also, the neutral curve for the most unstable mode, as shown in Fig. 3(a), gives $Re_{cr} = 519.018$ and $\beta_{cr} = 0.12$ that is identical with previously published results. This validates the present formulation and the method of linear stability analysis.

In Fig. 3(b), the neutral curve for the assisting flow with $Ri_x = 0.01$ is shown, giving $Re_{cr} = 589.3$ and corresponding $\beta_{cr} = 0.122$, that indicates stabilization of the assisting flow. In

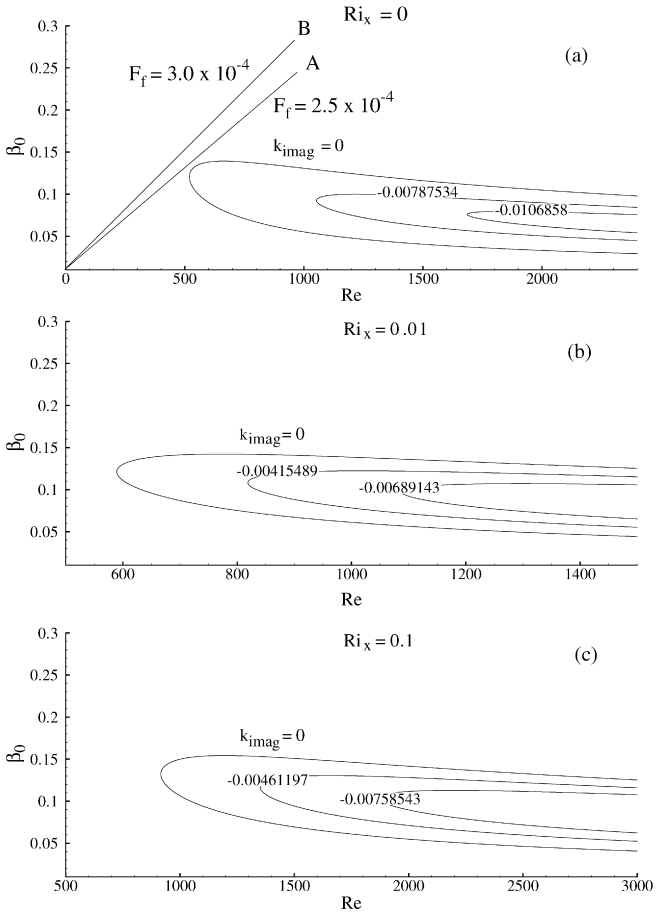

Fig. 3. Spatial amplification contours shown in $(Re - \beta_0)$ plane for assisting flows for indicated values of Ri_x. The neutral curves ($k_{imag} = 0$) are the outermost contours. Note the rays OA and OB in (a) are chosen for which simulation results are reported in Fig. 11.

Fig. 3(c), the neutral curve for assisting flow with $Ri_x = 0.1$ is shown, that indicates further stabilization with $Re_{cr} = 916.0$ and $\beta_{cr} = 0.133$. This type of alteration of stability properties by buoyancy effects have been reported by other investigators for assisting flows. However, quantitative values of growth and decay rates vary significantly. This can be attributed to different methods used to solve stability equations. We also note that for the case of Fig. 3(c), as the value of $Ri_x = 0.1$ is large, one should include second order perturbation terms in the mean flow representation of Eqs. (8) and (11), to investigate the variation of stability properties with retention of perturbation terms. However, when this was performed, no differences for either the eigen-spectrum or the neutral curve was found even for this large value of Ri_x.

In Fig. 4(a), the neutral curve is shown for opposing flow with $Ri_x = 0.01$ that indicates $Re_{cr} = 440.5$ and $\beta_{cr} = 0.123$, i.e. a destabilization of the flow in comparison with $Ri_x = 0$ case. In this figure, we have marked two straight lines originating from the origin and they represent the path taken by constant physical-frequency disturbances, that will be used for direct simulation of Navier–Stokes and energy equations in the next section. When Ri_x is increased to 0.02, Re_{cr} further reduces to $Re_{cr1} = 359.5$, while β_{cr1} increases to 0.129—indicating fur-

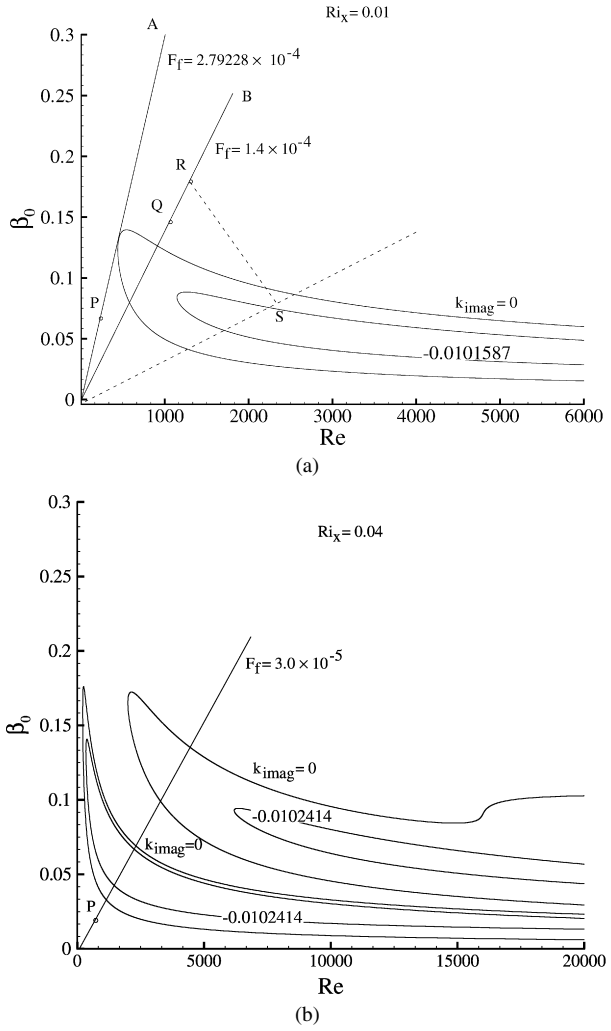

Fig. 4. (a) Spatial amplification contours shown in $(Re-\beta_0)$ plane for opposing flow with $Ri_x = 0.01$. The neutral curve ($k_{imag} = 0$) is indicated by the outer contour. The rays OA and OB are for the constant frequency wall-excitation cases, results of which are shown in Figs. 7(a) and 7(b). The points P and Q correspond to the middle of the wall-exciter. (b) Spatial amplification contours shown in $(Re-\beta_0)$ plane for opposing flow with $Ri_x = 0.04$. The neutral curves ($k_{imag} = 0$) are indicated by the outer contours. The ray from the origin corresponds to a constant frequency wall-excitation case result of which is shown in Fig. 8. Point P correspond to the middle of the wall-exciter.

Table 1
Critical parameters for assisting flows

Case	Ri_x	Re_{cr}	β_{cr}
1	0.0	519.018	0.120
2	0.001	526.529	0.121
3	0.01	589.30	0.122
4	0.1	916.0	0.133

ther destabilization at higher frequencies. Such deterioration of stability properties for opposing flows have been noted by Lee et al. [12] due to buoyancy effects. However, presence of two distinct lobes of the neutral curve for opposing flows for $Ri_x \geqslant 0.02$, has not been reported before. Lee et al. [12] indicated two maxima for the growth rate versus streamwise distance plot, without distinct lobes in the neutral curve—as shown

Table 2
Critical parameters for opposing flows

Case	Ri_x	Re_{cr1}	Re_{cr2}	β_{cr1}	β_{cr2}
1	0.0001	518.2	–	0.120	–
2	0.001	511.3	–	0.120	–
3	0.01	440.5	–	0.123	–
4	0.02	359.5	7705.3	0.129	0.0799
5	0.03	283.6	3747.4	0.137	0.118
6	0.035	248.2	2714.8	0.145	0.139
7	0.04	215.29	1996.0	0.154	0.165

here. According to them, the two maxima are due to the presence of two distinct unstable modes. Presence of two lobes of the neutral curve here implies presence of two Re_{cr} and β_{cr}. For $Ri_x = 0.02$, we have already noted one such pair, the other pair is given by, $Re_{cr2} = 7705.3$ and $\beta_{cr2} = 0.0799$. These critical parameters for opposing flow are given in Table 2.

Two lobes of neutral curve in Fig. 4(b) for $Ri_x = 0.04$ case give two critical Reynolds numbers $Re_{cr_1} = 215.29$ and $Re_{cr_2} = 1996.0$, while the corresponding critical circular frequencies are $\beta_{cr_1} = 0.154$ and $\beta_{cr_2} = 0.165$. We note that with increasing value of Ri_x, both the critical Reynolds numbers decrease continuously, with the second one decreasing rather sharply. From Table 2, we note that β_{cr_1} increases from 0.120 to 0.154 for $0.0001 \leqslant Ri_x \leqslant 0.04$ and β_{cr_2} increases from 0.0799 to 0.165 for $0.02 \leqslant Ri_x \leqslant 0.04$. Presence of multilobe neutral curves have also been shown for mixed convection flow over horizontal plate in Sengupta and Venkatasubbaiah [8]. The common features of multiple lobes in the neutral curves for mixed convection flows past horizontal and vertical plates at low speeds are due to higher order of the system, caused by the coupling of momentum and energy equations.

4. Direct numerical simulation

Stability results presented in the previous section are for parallel boundary layer developing over a vertical plate, obtained after linearizing the governing equations. In the process, we report the presence of distinct two-lobed neutral curve for opposing flows for the most unstable mode. It is pertinent to investigate this further, without being restricted by linear and parallel flow approximations. Also, all linear stability analysis suffers from the normal mode approach, i.e. the various modes present are sought separately and their actions are considered to be independent of each other. This can be rectified by the receptivity approach—as in Sengupta et al. [20] for the linearized response or by solving the Navier–Stokes equation with respect to specific excitation. In the following, we follow the latter by performing a direct simulation of the 2D flow field. The Navier–Stokes equations for incompressible flows are solved in stream function (ψ) and vorticity (ω) formulation. The governing equations (1) to (3) are written in $(\psi-\omega)$ formulation in an orthogonally transformed plane as given by,

$$\frac{\partial}{\partial\xi}\left(\frac{h_2}{h_1}\frac{\partial\psi}{\partial\xi}\right)+\frac{\partial}{\partial\eta}\left(\frac{h_1}{h_2}\frac{\partial\psi}{\partial\eta}\right)=-h_1h_2\omega \tag{40}$$

$$h_1h_2\frac{\partial\omega}{\partial t}+\frac{\partial\psi}{\partial\eta}\frac{\partial\omega}{\partial\xi}-\frac{\partial\psi}{\partial\xi}\frac{\partial\omega}{\partial\eta}$$
$$=\mp\frac{Gr}{Re^2}\left(\frac{\partial h_1T}{\partial\eta}\right)+\frac{1}{Re}\left[\frac{\partial}{\partial\xi}\left(\frac{h_2}{h_1}\frac{\partial\omega}{\partial\xi}\right)+\frac{\partial}{\partial\eta}\left(\frac{h_1}{h_2}\frac{\partial\omega}{\partial\eta}\right)\right] \tag{41}$$

$$h_1h_2\frac{\partial T}{\partial t}+\frac{\partial\psi}{\partial\eta}\frac{\partial T}{\partial\xi}-\frac{\partial\psi}{\partial\xi}\frac{\partial T}{\partial\eta}$$
$$=\frac{1}{RePr}\left[\frac{\partial}{\partial\xi}\left(\frac{h_2}{h_1}\frac{\partial T}{\partial\xi}\right)+\frac{\partial}{\partial\eta}\left(\frac{h_1}{h_2}\frac{\partial T}{\partial\eta}\right)\right] \tag{42}$$

where ξ, η are coordinates in transformed plane and h_1, h_2 are the scale factors given by, $h_1=(x_\xi^2+y_\xi^2)^{1/2}$ and $h_2=(x_\eta^2+y_\eta^2)^{1/2}$, for the orthogonal mapping used here. The governing equations, in terms of ψ and ω, are given in Arpaci and Larsen [21] in Cartesian frame. Representation of the same in an orthogonally mapped plane is easily performed (not shown here) to finally obtain the equations given above. Various non-dimensionalizations remain the same, as in Section 2. In Section 3, the length scale (L) was chosen as the displacement thickness, a quantity that varied with streamwise distance. In this section, a reference length would instead be chosen as a constant, to be fixed later.

4.1. Boundary and initial conditions

Specification of proper boundary conditions and their implementation into the numerical method is an issue of great importance in DNS. To obtain higher resolution and easily implement boundary conditions, we compute the equations in the orthogonally transformed ($\xi-\eta$)-plane, obtained from the Cartesian frame via the transformations given by,

$$x(\xi)=x_{in}+L_D\left[1-\frac{\tanh[\beta_1(1-\xi)]}{\tanh\beta_1}\right] \tag{43}$$

$$y(\eta)=L_h\left[1-\frac{\tanh[\beta_1(1-\eta)]}{\tanh\beta_1}\right] \tag{44}$$

with $0\leqslant\xi,\eta\leqslant1$. In the above, x_{in} is the streamwise coordinate of the inflow of the computational domain whose streamwise extent is given by $L_D=x_{\text{out}}-x_{\text{in}}$, where x_{out} is the location of the outflow of the computational domain—taken as either $6L$ or $12L$-depending upon the problem solved. Similarly, the second transformation relates the wall-normal physical distance of L_h to the transformed co-ordinate η. Here, we have used $\beta_1=2$ to obtain desired grid clustering near the inflow and the wall. A very localized wall-excitation is applied at a location near the inflow and for this reason the grid clustering in its vicinity is required. This type of tangent hyperbolic transformation apart from producing desired grid clustering, also helps in reducing aliasing error and is widely used in simulations.

In the above equations, dependent variables represent total quantities composed of primary and disturbance component. In the following, we discuss the boundary conditions separately—so that the process of obtaining the mean and disturbance flow are clearly revealed. For the disturbance flow, these boundary conditions reveal the nature of applied excitation at the wall. However, the boundary conditions for Eqs. (40) to (42) will be used for the total variable for the receptivity calculations. At the inflow and on the top of the domain, free stream boundary conditions for the primary flow are applied as,

$$T=0;\qquad\frac{\partial\psi}{\partial\eta}=h_2,\qquad\omega=0 \tag{45}$$

Similarly, the required boundary conditions for the primary flow at the wall are,

$$T=1;\qquad\psi=constant,\qquad\omega=-\frac{1}{h_2^2}\frac{\partial^2\psi}{\partial\eta^2} \tag{46}$$

For the disturbance quantities at the wall, we use the no-slip along with a permeable-wall time-dependent condition, that represents a simultaneous blowing and suction on a localized strip to generate waves (as in Fasel and Konzelmann [15]). Corresponding unsteady disturbance flow conditions for non-dimensional variables are given as,

$$u_d=0,\qquad v_d=A_m\sin(\beta t),\qquad T_d=0 \tag{47}$$

where β is the non-dimensional disturbance frequency and A_m is amplitude of the disturbance. The amplitude function is defined along the blowing and suction strip, for $x_1\leqslant x\leqslant x_{st}$ (as given in Fasel and Konzelmann [15]):

$$A_m=15.1875\left(\frac{x-x_1}{x_{st}-x_1}\right)^5-35.4375\left(\frac{x-x_1}{x_{st}-x_1}\right)^4$$
$$+20.25\left(\frac{x-x_1}{x_{st}-x1}\right)^3 \tag{48}$$

And for $x_{st}\leqslant x\leqslant x_2$:

$$A_m=-15.1875\left(\frac{x_2-x}{x_2-x_{st}}\right)^5+35.4375\left(\frac{x_2-x}{x_2-x_{st}}\right)^4$$
$$-20.25\left(\frac{x_2-x}{x_2-x_{st}}\right)^3 \tag{49}$$

where $x_{st}=(x_1+x_2)/2$; with x_1 and x_2 representing the beginning and end of the streamwise extent of the strip.

This distribution produces clean localized vorticity disturbances. The disturbance generation employing blowing and suction strip, represents spatial downstream development of disturbance waves, as originally observed in laboratory experiments for flows without heat transfer [16].

At the outflow, boundary conditions for the total variables are given by,

$$\frac{\partial v}{\partial x}=0;\qquad\frac{\partial\omega}{\partial t}+U_c\frac{\partial\omega}{\partial x}=0$$
$$\frac{\partial T}{\partial t}+U_c\frac{\partial T}{\partial x}=0 \tag{50}$$

where U_c is convective speed of the disturbances through the outflow and here it is taken as the free-stream speed.

For the numerical simulations performed here, results are obtained with a small amplitude of the disturbances at the wall to allow comparison with the results of linear stability theory. For the DNS study, we have chosen the parameters as $U_\infty=30$ m/s, $\nu=1.5\times10^{-5}$ m^2/s and $L=0.05$ m or 0.4 m for the cases with single and two-loop neutral curves depending

upon the value of Ri_x. Navier–Stokes equations (40) to (42), together with the boundary conditions specified above are solved using high accuracy compact scheme OUCS3, whose details are given in Sengupta et al. [22] and [23]. This, formally second order accurate scheme, is optimized for least error in the wave number plane while evaluating the nonlinear convection terms of the VTE (41). Further details on the basic scheme and boundary closures are given in [23]. For the fixed reference Reynolds number (Re_L) and Ri_x, Eqs. (40) to (42) are solved first with the boundary conditions specified for the primary flow to obtain the steady state solution.

The steady state solution is thereafter perturbed at the wall with the simultaneous blowing-suction disturbance of the type given in Eq. (47) for the fixed frequency parameter $F_f = \beta/Re_L$. Results are obtained with the amplitude reduced hundred times of that used in Fasel and Konzelmann [15] to allow comparison with the results of linear stability theory. For the Blasius boundary layer excitation that was investigated in [15], the linear stability analysis in Sengupta et al. [20] have shown the presence of only a few modes (less than four for moderate Reynolds numbers), with only one mildly unstable eigenvalue and the rest of them are all stable. In comparison, the mixed convection opposing flows past vertical plate are more unstable (as shown in Section 3) with significantly higher instability indicated by the growth rate that is two orders of magnitude higher. Also, near critical Reynolds number, many stable eigenvalues with similar attenuation rates cause modal interactions of the type described in [1,2]. These interactions give rise to additional spatio-temporal excitation—usually at lower frequency. These interactions lead to distortion, that may appear as nonlinear—but they are essentially linear in origin. It is for these reasons, the amplitude of excitation is taken as one-hundredth of the amplitude used in Fasel and Konzelmann [15] to compare with linear theory results, while obtaining perceptible response within the chosen computational domain.

To test the numerical method, we compute a case with $Re_L = 10^5$, $Ri_x = 0$ and $F_f = 1.4 \times 10^{-4}$, as in Fasel and Konzelmann [15] with the outflow boundary at $x_{\text{out}} = 6.0$ (corresponding Reynolds number based on displacement thickness δ^*, is $Re_{\delta^*} = 1333$) and the location of the top of the computational domain is at $L_h = 0.35$, i.e. $y^* = 32.3\delta^*$. We have used the tangent hyperbolic grid in streamwise and wall-normal direction with (800×300) points. These can be contrasted with the grid used in Fasel and Konzelmann [15], who took 68 uniformly distributed points in the wall-normal direction, up to a distance of $6\delta^*$ only. Disturbances are created at the wall as localized blowing and suction from a narrow strip located between $x_1 = 0.2$ and $x_2 = 0.5$, with the corresponding Reynolds number as $Re_{\delta^*} = 243.37$ and 384.8, respectively—as measured from the leading edge of the plate. For these excitation parameters and location, it is noted from Fig. 3(a) that the disturbances first decay before it enters in the region given by the neutral curve and amplify. Inside the neutral loop the disturbances amplify and they attenuate when they emerge out of the neutral curve. The computed disturbance streamwise velocity (u_d) and temperature (T_d), from the solution of Eqs. (40) to (42), are shown in Fig. 5(a) at a time when the unstable flow pattern is established and does not change further with time. In all the frames of Fig. 5, we have drawn two vertical lines that indicate the beginning and end of the unstable region given by the linear stability analysis for the chosen frequency. These informations are obtained by drawing the rays, as in Fig. 4, from the origin with the slope indicating the non-dimensional frequency F_f. The point of entry of this ray in the neutral loop locate the first vertical line, indicating the beginning of instability for that frequency and the point of exit from the neutral loop indicating the right vertical line. Results show good correspondence for the extent of the unstable region obtained by the linear stability analysis and the present DNS results for the cases with $Ri_x = 0$ and 0.0001 shown in Fig. 5(a) and (b). This validates the numerical method used here for mixed convection flow the DNS. In Fig. 5, all the frames are shown at $t = 30$ after starting the excitation in each case identically. Thus, the relative receptivity of the flows are ascertained by comparing the three cases shown in Fig. 5. In Fig. 5(b) and (c), u_d and T_d are plotted as function of x at $y^* = 0.648\delta^*$ for the opposing flows with $Ri_x = 0.0001$ and 0.01 for $F_f = 1.4 \times 10^{-4}$, respectively. One sees slightly higher amplitude for the case in Fig. 5(b) as compared to the case in Fig. 5(a), with buoyancy destabilizing the opposing flow. In Fig. 5(c), one notes the envelopes of u_d and T_d to show significantly higher amplitudes, as compared to that shown in Fig. 5(a) and (b). There are features of the flow that show differences between the results of linear stability analysis and DNS for this higher Ri_x case. Here, the match is only qualitative for the extent of the unstable regions as obtained by linear and nonlinear approaches. The extent is underestimated by the linear analysis as compared to DNS. In all the cases, excitation is applied near the leading edge of the plate, at identical locations and in its immediate vicinity the attenuating nature of disturbance field is not distinctly noticeable.

To provide a quantitative comparison between DNS and linear stability theory, we plot the growth rate as a function of streamwise distance for $Ri_x = 0.0$ and $F_f = 1.4 \times 10^{-4}$-case in Fig. 6. In the figure, A_0 represents the initial amplitude of disturbances, taken here at $x_i = 1.9454$ from where DNS indicated continuous growth. From the amplitude envelope we have calculated $A(x)$ to obtain the quantity in the ordinate of the figure. For the linear theory, the corresponding ordinate is obtained from Eq. (12) for the amplitude as,

$$\frac{A(x)}{A_0(x_i)} = e^{-\int_{x_i}^{x} k_i \, dx} \tag{51}$$

Fig. 6 indicates detailed similarity and differences for the DNS and linear stability calculations. Similar comparisons between DNS and linear theory were also shown in Seifert and Tumin [24] for different excitation frequencies. They noted differences increasing with frequency of excitation.

To test the critical parameters obtained from the linear stability analysis, we compute a case for $F_f = 2.79228 \times 10^{-4}$ (the non-dimensional excitation frequency), that was marked in Fig. 4(a) as OA, touching the critical point, without entering the unstable region—for the opposing flow case with $Ri_x = 0.01$. The solution to Eqs. (40) to (42) are obtained and u_d is plotted as a function of x in Fig. 7(a), for a fixed height of

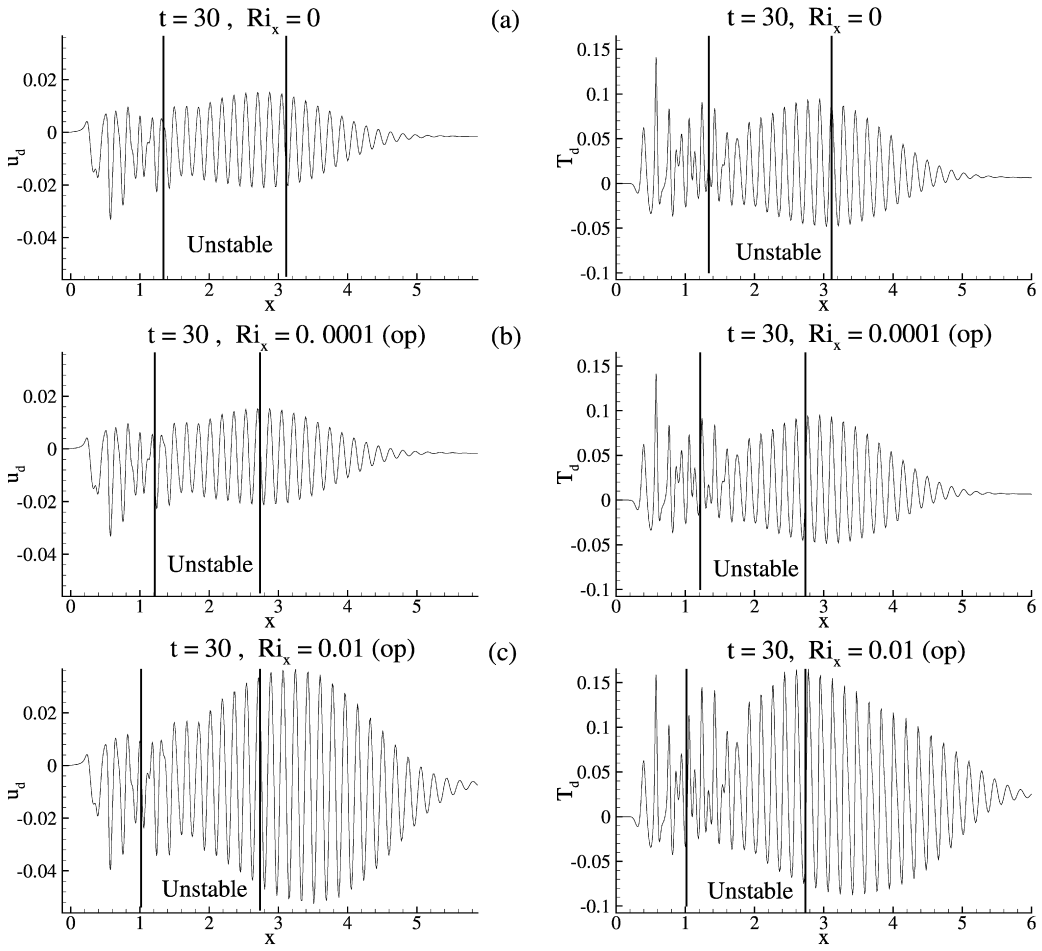

Fig. 5. Disturbance quantities u_d and T_d versus x at $y^* = 0.648\delta^*$ with $F_f = 1.4 \times 10^{-4}$ excitation. Results are shown after the transients are gone and a time periodic state is reached for (a) $Ri_x = 0$; (b) opposing flow with $Ri_x = 0.0001$ and (c) opposing flow with $Ri_x = 0.01$.

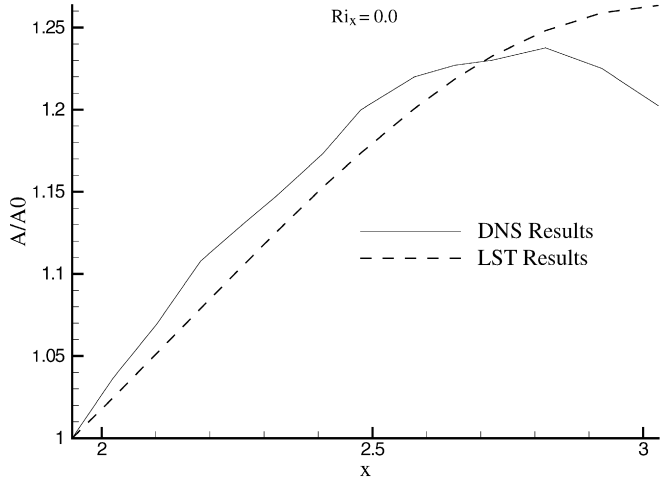

Fig. 6. Comparison of growth rates calculated from linear instability theory (LST) and direct numerical simulation (DNS) for the case shown in Fig. 5(a) for $Ri_x = 0.0$.

$y^* = 0.648\delta^*$. The exciter is located at the same location, as in the case of Fig. 5. Here, as well as in Fig. 5, excitation causes a local solution that is indicated by high amplitude fluctuation, followed by the asymptotic solution—as given by the stability analysis. From Fig. 7(a), this asymptotic part is seen as the small amplitude decaying wave solution. As compared to the case shown in Fig. 5(c), here the disturbance remain all the time in the damped region except when it touches the neutral curve at a single point. This type of continuously decaying solution is seen to occur at the lowest possible frequency—providing the critical circular frequency. This calculation validates the critical frequency obtained from the linear stability results of Table 2. Another interesting phenomenon is also seen from the results of DNS reported here. This relates to the spatio-temporal growing wave-front shown in Fig. 7(a). This type of spatio-temporal growing wave-front has been reported also in Sengupta et al. [1] for a pure hydrodynamic stability study, where the phenomenon was established to be related to interactions of multiple decaying modes for spatially stable systems. Presented results in Fig. 7(a) shows that this event is also present for mixed convection flows. From the plotted figures at $t = 5$ and $t = 8$, one notes this leading wave-front to move like a packet in the downstream direction, with the amplitude continuously increasing. To show this phenomenon to be generic, we performed another simulation for $Ri_x = 0.01$, for which the exciter is at a location beyond the upper branch of the neutral curve. Corresponding constant physical frequency line was identified as OB in Fig. 4(a). In Fig. 7(b), u_d is plotted as a function of x at $y^* = 0.648\delta^*$ for this opposing flow case excited by a non-dimensional fre-

quency, $F_f = 1.4 \times 10^{-4}$. In this case, location of the blowing and suction strip is given by $x_1 = 3.234$ (corresponding $Re_{\delta*} = 1000$) and $x_2 = 3.5$ (corresponding $Re_{\delta*} = 1040.31$).

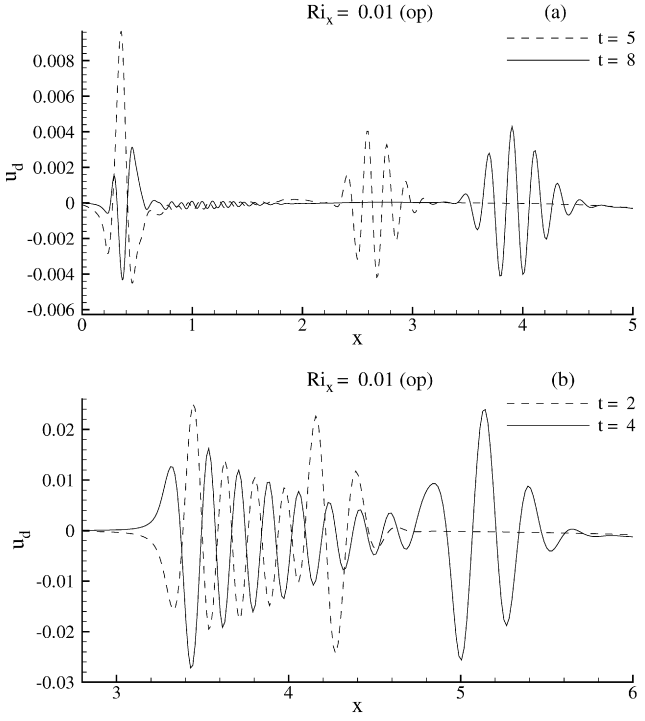

Fig. 7. Disturbance velocity u_d versus x at $y^* = 0.648\delta^*$ for opposing flow with $Ri_x = 0.01$, excited at the wall by frequencies given by (a) $F_f = 2.79228 \times 10^{-4}$ and (b) $F_f = 1.4 \times 10^{-4}$.

In this case, following the local solution, the asymptotic part of the excitation field is seen also as a decaying wave. In comparison to the case of Fig. 7(a), here the damping rates are much lower and thus, the asymptotic part of the solution is seen over a longer streamwise stretch. The displayed solutions at $t = 2$ and $t = 4$, once again show the leading spatio-temporally growing wave-front. Thus, the spatio-temporal growing wave-front is seen to occur due to interaction of multiple modes for fluid flows—with or without heat transfer. The spatio-temporal wave-front seen here is the same that was described in [1,2] for the Blasius profile. It is not a transient response—as established in Sengupta et al. [1,2] by solving the problem using both linear receptivity approach and solution of full Navier–Stokes equation. In the linear receptivity study, governing Orr–Sommerfeld equation was solved by Bromwich contour integral method described in [2,20]. The establishment of the presence of spatio-temporal growing wave-front is worthwhile, as it can explain discrepancies between experimental observation and normal-mode linear stability theory results. We noted in [1,2] and once again here that the leading wave-packet displays variation at lower wave numbers and frequencies as compared to the asymptotic waves. This has an important significance. For illustration purpose, let us consider the case where the shear layer is excited by a constant frequency—as indicated by the line OB in Fig. 4(a). If the center of the asymptotic solution has reached a streamwise distance indicated by R, then the leading wave-packet would be ahead of this, say at a point S, where the flow experiences an excitation corresponding to the time-scale of the wave-front. The point S can be inside the neutral loop, even though the operational point R is outside the neutral

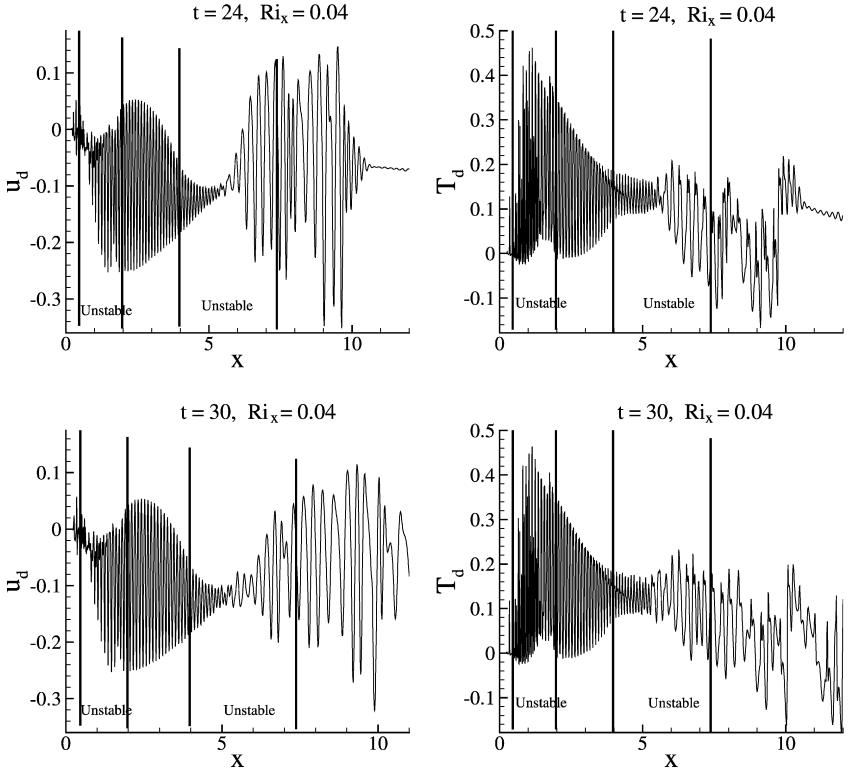

Fig. 8. Disturbance quantities u_d and T_d versus x at $y^* = 0.68126\delta^*$ for excitation at $F_f = 3.0 \times 10^{-5}$, for opposing flow with $Ri_x = 0.04$.

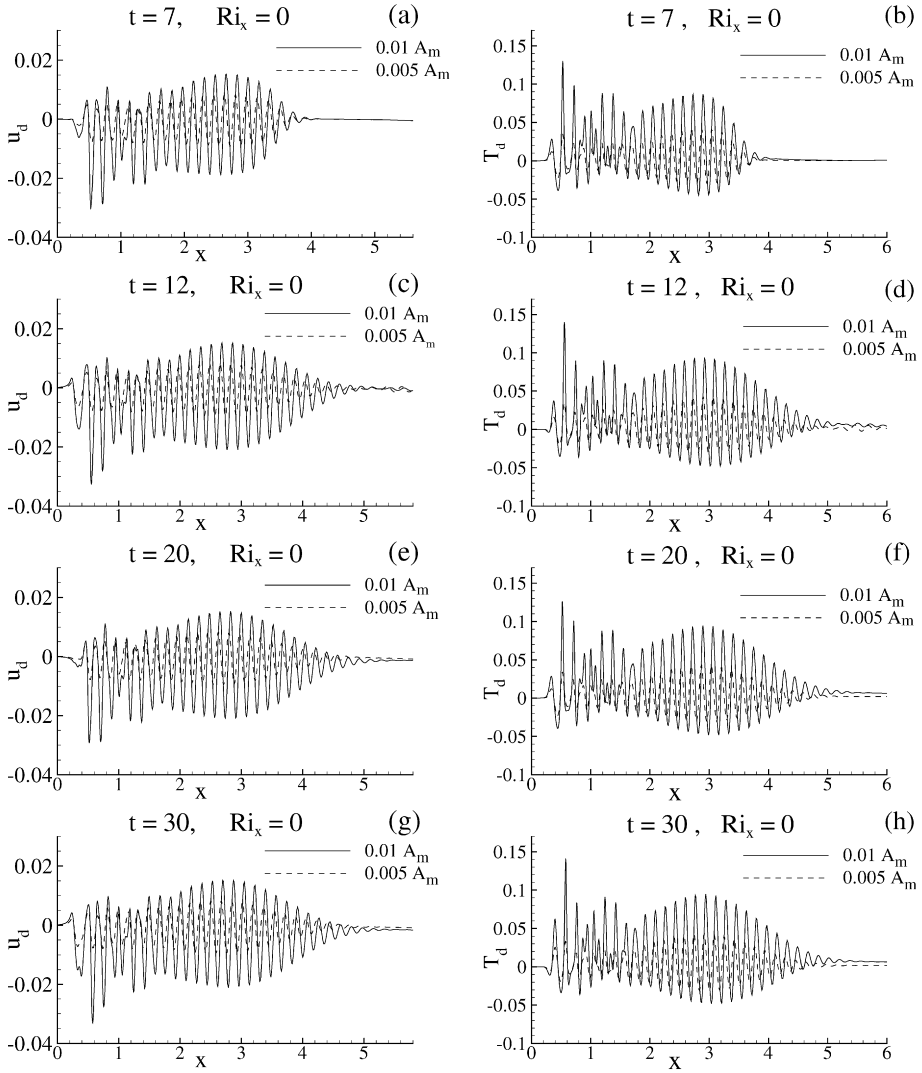

Fig. 9. Disturbance quantities u_d and T_d versus x at $y^* = 0.648\delta^*$ for excitation at $F_f = 1.4 \times 10^{-4}$, for the case of $Ri_x = 0.0$ at the indicated times.

loop—as indicated in Fig. 4(a). Thus, the normal mode analysis would indicate the boundary layer to be stable, while the leading wave-packet would indicate instability. Once excited, the leading wave-packet continues to exist. This is not a transient and the resultant behavior cannot be interpreted by the normal-mode linear instability theory. However, a receptivity approach, as in [1,2,20], based on linearized analysis can do so. Also, an appropriate DNS like the present one can explain the same.

To explain special features of mixed convection boundary layers, like the existence of double loop in the neutral curve for opposing flows, we have computed another case for $Re_L = 8.0 \times 10^5$, $Ri_x = 0.04$ and $F_f = 3.0 \times 10^{-5}$ with the location of outflow boundary at $x_{\text{out}} = 12.0$ where the corresponding $Re_{\delta^*} = 5798.44$. The top of the computational domain is located here at $L_h = 0.2$, i.e. at $y^* = 27.59\delta^*$ with 1600 points in the streamwise direction and 300 points in the wall-normal direction used for the computation. Here, the blowing and suction strip is located between $x_1 = 0.2$ (corresponding $Re_{\delta^*} = 748.57$) and $x_2 = 0.3$ (corresponding $Re_{\delta^*} = 916.81$). Numerically obtained u_d and T_d are plotted against x at $y^* = 0.68126\delta^*$ in Fig. 8. In this figure, the linearly unstable regions have been marked again by vertical lines. The two sets of lines correspond to two loops traversed by a single constant frequency disturbance—as shown in Fig. 4(b). From Fig. 8, existence of a double-loop for the neutral curve is seen qualitatively only and the extent of stable and unstable region in the streamwise direction matches only for the lower loop, while the upper loop match is not clear. This is due to the traveling waves propagating downstream exhibit interaction of the thermal mode (upper loop) with the hydrodynamic mode (lower loop mode). Also, due to the occurrence of multiple wave-packets caused by the dominant hydrodynamic and thermal modes makes the signal to be multi-periodic—even for the single frequency excitation—as was the case for $Ri_x = 0$ shown in Fig. 5(a). Also, the amplitude of variation for T_d drastically increases with Ri_x for opposing flow. This shows the buoyancy effects to severely destabilize opposing flows, as affected significantly by nonlinear effects.

To resolve the issue of linear and non-linear nature of the disturbance field as obtained by DNS, we have performed two

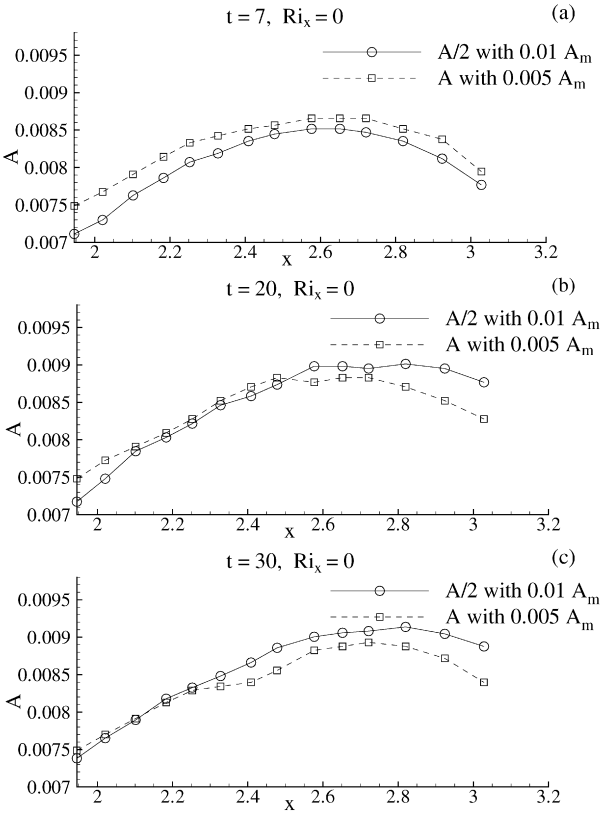

Fig. 10. Amplitude envelope of u_d versus x for the case of Fig. 9, shown for three times. Note that the output is scaled by the same ratio, as the input ratio.

additional calculations for $Ri_x = 0.0$ case with amplitudes of $0.01A_m$ and $0.005A_m$, with A_m as defined in Eqs. (48) and (49). In Fig. 9, the results are compared between the two cases at four discrete times. It is clearly noted that the asymptotic part of the solution reduces when the amplitude of the blowing-suction type excitation is reduced. To ascertain whether these cases represent linear dynamics or not, in Fig. 10, the amplitude envelope is compared after the higher amplitude excitation case results are scaled by a factor of two—this being the ratio of the input to the system. Despite the nonlinear and nonparallel nature of the governing equation, the plotted scaled results in Fig. 10 shows linear nature of the response of the system.

Finally, the issue of the spatio-temporal wave front is investigated to establish the correct nature of its genesis. In [1] the analysis for it was made for parallel shear layer and it was noted that the wave front originates due to the interaction of multiple modes and they were clearly visible for spatially stable systems. The leading edge of spatially stable and unstable cases were exactly at identical locations with identical shape (as in Fig. 3 of that reference), it is tempting to conclude that *this is due to the initial transients corresponding to a packet created with the maximum growth rate of the parallel shear layer at that Reynolds number*. This was further explained in [25] where the leading wave fronts for the two spatially stable cases were analyzed for $Re = 1000$ with (a) $\beta_0 = 0.05$ and (b) $\beta_0 = 0.15$. These two frequencies correspond to below and above the neutral curve for $Re = 1000$ and the fast Fourier transform of the signal at a fixed large time revealed the wavenumbers corresponding to the wave fronts to be very different.

To explain this aspect further for actual shear layers including nonlinear and nonparallel nature of instability, we computed two more cases for Blasius boundary layer ($Ri_x = 0.0$) with the exciter located between x_1 and x_2, where the Reynolds numbers, based on local displacement thickness, are 400 and 450, respectively. Also, the frequencies of excitation are chosen as $F_f = 2.5 \times 10^{-04}$ and 3.0×10^{-04}. The reason for choosing these frequencies is that the created disturbances would not go inside the neutral loop—as shown by the two rays OA and OB in Fig. 3(a). Thus, the disturbances are created at locations where the shear layer is sub-critical and the subsequently they would not be unstable from linear theory point of view, as they convect downstream. In spite of this, if a spatio-temporal wave front is created, then the italicized hypothesis given in the previous paragraph is incorrect. In Fig. 11, the solutions for these two cases are shown at discrete times and one can clearly see the presence of leading wave fronts for both the cases. The main wave-packet is due to the instability of the shear layer near the exciter where the neutral curve is different from that given by the linear instability of the parallel shear layer. This demonstrate the nonparallel effects to be significant at high frequencies, as has been postulated earlier in the literature. The properties of wave fronts for these two frequencies are also different-once again repudiating the italicized comment of the last paragraph.

5. Summary

To study the linear stability of mixed convection flows past vertical plate, one requires a method to obtain it as a parallel flow. These equations have been obtained using new variables in Eqs. (4) and (5), with the small buoyancy effect modeled by Boussinesq approximation, given by the term involving the buoyancy parameter Ri_x, in the momentum equation. As Ri_x is small, a regular perturbation method is used to obtain the mean flow, shown in Fig. 2. Retaining second order terms do not change the equilibrium flow, whose effects have also been tested here on the stability property. The linear spatial stability of the equilibrium flow is investigated here using the compound matrix method, for mixed convection flow past vertical plate. Results are shown as neutral curves in Figs. 3 and 4 for assisting and opposing flows for different values of Ri_x. Results for the assisting flows in Fig. 3, display increasing stability with increasing assisting buoyancy—as reported by other researchers also.

A double loop of the neutral curve has been shown here, for the first time for mixed convection opposing flows, in the limit of $Ri_x \geqslant 0.02$. The neutral curve shown in Fig. 4(b), clearly displays presence of two distinct lobes of the neutral curve. Presence of two loops give rise to two sets of critical Reynolds numbers and circular frequencies. We note that due to coupling of momentum and energy equation, the order of the system increases, that increases the number of modes for flows with heat transfer, as compared to only very few modes for flows without heat transfer.

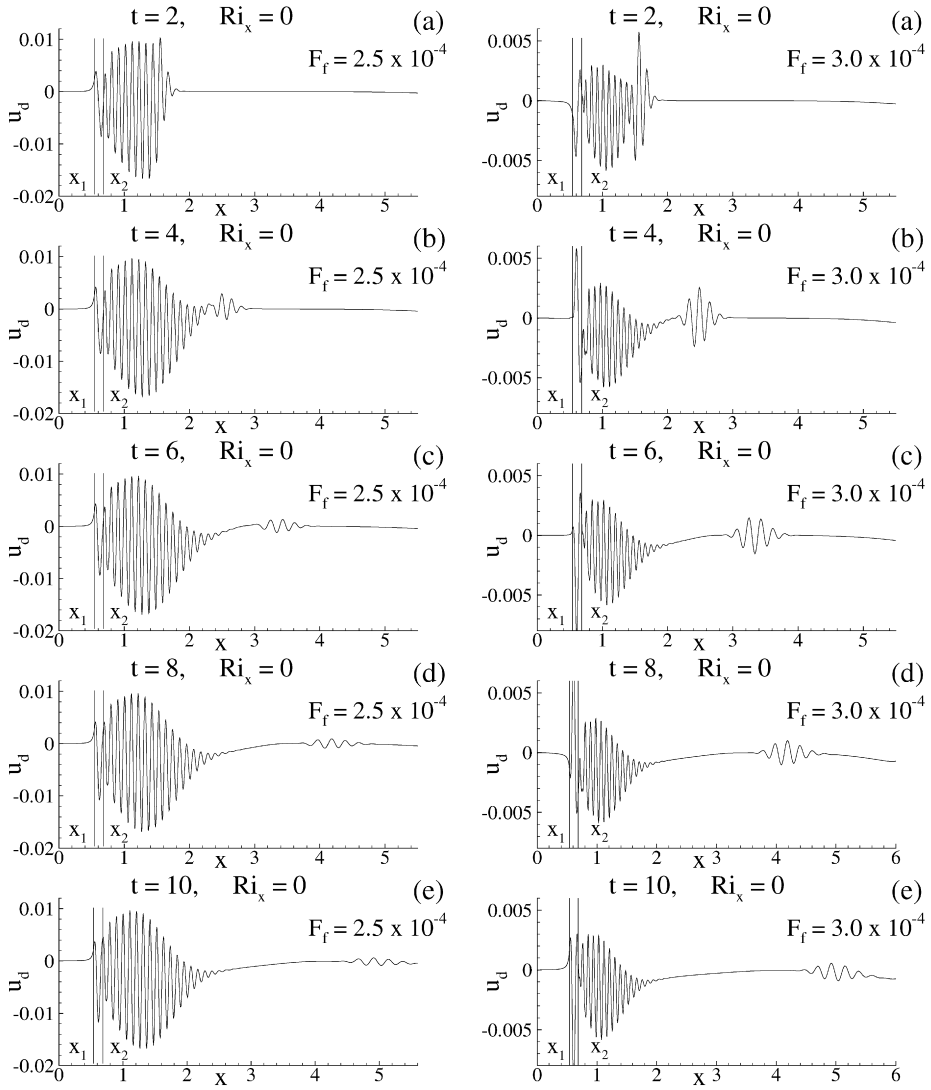

Fig. 11. Disturbance quantity u_d versus x at $y^* = 0.648\delta^*$ for excitation at $F_f = 2.5 \times 10^{-4}$ (Shown on left column) and $F_f = 3.0 \times 10^{-4}$ (Shown on the right column), for $Ri_x = 0.0$ at the indicated times. Note the rays OA and OB in Fig. 3 correspond to these cases shown here.

To verify the observations of the linear analysis and to investigate the nonlinear and nonparallel nature of flow stability, two-dimensional Navier–Stokes and energy equations have been solved here by an accurate method, when the boundary layer is excited by harmonic simultaneous suction and blowing at the wall. This kind of receptivity study via solution of Navier–Stokes equation have been reported for flows without heat transfer in Fasel and Konzelmann [15] and Sengupta et al. [1]. While Fasel and Konzelmann [15] have shown the excitation of unstable Tollmien–Schlichting waves; in Sengupta et al. [1] this was done for both stable and unstable systems, displaying a leading wave-front. The present effort is an attempt to establish the same for mixed convection flows for the first time and to verify the features of linear stability studies. The linear stability analysis features of the flow are clearly seen in the DNS results. Such similarities are also noted for the opposing flow case of $Ri_x = 0.0001, 0.01$, shown in Fig. 5(b) and (c). In Fig. 6, we have compared the growth rate calculated by linear stability theory and by DNS, for the case of Fig. 5(a).

We also establish the presence of spatio-temporal growing wave front for mixed convection flows, extending similar observation in the study by Sengupta et al. [1,2] for Blasius boundary layer. Results are shown in Fig. 7, for $Ri_x = 0.01$ for two frequencies of wall excitation. In the first case, the frequency is chosen in such a manner that the constant frequency line is tangential to the tip of the neutral curve—such that the created disturbance is always attenuated. This shows up as a severely attenuated traveling wave that is preceded by a spatio-temporal growing wave front. This result is shown in Fig. 7(a). In Fig. 7(b), a higher frequency is chosen, but the location of the disturbance source is where the created waves are attenuated by a lesser degree, as compared to the case of Fig. 7(a). Here also, one sees a spatially decaying wave, preceded by the spatio-temporal growing wave-front. In Fig. 8, time evolution of disturbance field is shown for the disturbance streamwise velocity and temperature field for opposing flow with $Ri_x = 0.04$, for which the neutral curve in Fig. 4(b) show two loops of the neutral curve. Here, wall excitation is applied before the beginning

of the first unstable loop. Presented results show two streamwise stretches where the disturbances amplify. The length of these stretches match only qualitatively with the linear stability results, while the differences are due to nonlinear and nonparallel effects. However, the results shown in Figs. 9 and 10, clearly indicates that the influence of nonlinearity is rather very small, for the case of $Ri_x = 0.0$ for the chosen frequency and amplitude levels.

The results shown in Figs. 9 to 11, explain further the nature of the disturbance field computed via DNS, focusing upon the nonlinear and nonparallel nature of the flow instability with and without heat transfer.

References

[1] T.K. Sengupta, A.K. Rao, K. Venkatasubbaiah, Spatio-temporal growing wave-fronts in spatially stable boundary layers, Phys. Rev. Lett. 96 (224504) (2006) 1–4.
[2] T.K. Sengupta, A.K. Rao, K. Venkatasubbaiah, Spatio-temporal growth of disturbances in a boundary layer and energy based receptivity analysis, Phys. of Fluids 18 (094101) (2006) 1–9.
[3] P.G. Drazin, W.H. Reid, Hydrodynamic Stability, Cambridge Univ. Press, Cambridge, UK, 1981.
[4] B. Gebhart, Y. Jaluria, R.L. Mahajan, B. Sammakia, Buoyancy-Induced Flows and Transport, Hemisphere Publication, Washington, DC, 1988.
[5] R.A. Brewstar, B. Gebhart, Instability and disturbance amplification in a mixed -convection boundary layer, J. Fluid Mech. 229 (1991) 115–133.
[6] R.S. Wu, K.C. Cheng, Thermal instability of Blasius flow along horizontal plates, Int. J. Heat Mass Transfer 19 (1976) 907–913.
[7] T.S. Chen, A. Mucoglu, Wave instability of mixed convection flow over a horizontal flat plate, Int. J. Heat Mass Transfer 22 (1979) 185–196.
[8] T.K. Sengupta, K. Venkatasubbaiah, Spatial stability for mixed convection boundary layer over a heated horizontal plate, Studies in Applied Mathematics 117 (3) (2006) 265–298.
[9] X.A. Wang, An experimental study of mixed, forced, and free convection heat transfer from a horizontal flat plate to air, ASME J. Heat Transfer 104 (1982) 139–144.
[10] A. Mucoglu, T.S. Chen, Wave instability of mixed convection flow along a vertical flat plate, Num. Heat Transfer 1 (1978) 267–283.
[11] P. Moresco, J.J. Healey, Spatio-temporal instability in mixed convection boundary layers, J. Fluid Mech. 402 (2000) 89–107.
[12] S.L. Lee, T.S. Chen, B.F. Armaly, Wave instability characteristics for the entire regime of mixed convection flow along vertical flat plates, Int. J. Heat Mass Transfer 30 (8) (1987) 1743–1751.
[13] L. Allen, T.J. Bridges, Numerical exterior algebra and the compound matrix method, Numer. Math. 92 (2002) 197–232.
[14] L. Allen, T.J. Bridges, Hydrodynamic stability of the Ekman boundary layer including interaction with a compliant surface: a numerical frame work, European J. Mechanics B/Fluids 22 (2003) 239–258.
[15] H. Fasel, U. Konzelmann, Non-parallel stability of a flat-plate boundary layer using the complete Navier–Stokes equations, J. Fluid Mech. 221 (1990) 311–347.
[16] G.B. Schubauer, H.K. Skramstad, Laminar boundary layer oscillations and the stability of laminar flow, J. Aero. Sci. 14 (2) (1947) 69–78.
[17] S.L. Lee, T.S. Chen, B.F. Armaly, Non-parallel wave instability of mixed convection flow on inclined flat plates, Int. J. Heat Mass Transfer 31 (7) (1988) 1385–1398.
[18] A. Tumin, The spatial stability of natural convection flow on inclined plates, ASME J. Fluid Engng. 125 (2003) 428–437.
[19] P.H. Oosthuizen, D. Naylor, An Introduction to Convective Heat Transfer Analysis, McGraw Hill Int. Edn., New York, USA, 1999.
[20] T.K. Sengupta, M. Ballav, S. Nijhawan, Generation of Tollmien–Schlichting waves by harmonic excitation, Phys. of Fluids 6 (3) (1994) 1213–1222.
[21] V.S. Arpaci, P.S. Larsen, Convective Heat Transfer, Prentice-Hall, Englewood Cliffs, NJ, 1984.
[22] T.K. Sengupta, S.K. Sircar, A. Dipankar, High accuracy schemes for DNS and acoustics, J. Sci. Comput. 26 (2) (2006) 151–193.
[23] T.K. Sengupta, G. Ganeriwal, S. De, Analysis of central and upwind compact schemes, J. Comput. Phys. 192 (2003) 677–694.
[24] A. Seifert, A. Tumin, Nonlinear localized disturbances in an adverse pressure gradient boundary-layer transition: Experiment and linear stability analysis, in: Prog. in Fluid Flow Research: Turbulence and Applied MHD (Editor-in-Chief: P. Zarchan), Prog. in Astronautics and Aeronautics Series 182 (1998) 3–13.
[25] T.K. Sengupta, A.K. Rao, Spatio-temporal receptivity of boundary layers by Bromwich contour integral method, in: G. Lube, G. Rapin (Eds.), Proc. of Boundary and Interior Layers; BAIL 2006 Conf. Held at Univ. of Goettingen, Germany, 2006.